

Cite this: *Energy Environ. Sci.*,
2022, 15, 771

Evolution of a solid electrolyte interphase enabled by FeN_x/C catalysts for sodium-ion storage†

Huicong Xia,^{ab} Lingxing Zan,^{bc} Gan Qu,^a Yunchuan Tu,^b Hongliang Dong,^d
Yifan Wei,^a Kaixin Zhu,^b Yue Yu,^a Yongfeng Hu,^e Dehui Deng^{*b} and
Jianan Zhang^{id} ^{*a}

The structure and chemical engineering of a solid electrolyte interphase (SEI) play a vital role in rechargeable batteries. The underlying correlation between the properties of the enhanced sodium (Na) ion storage and SEIs in metal–nitrogen (MN_x) platform electrodes was not revealed during charging and discharging cycles. Herein, the capacity enhancement of FeN_x/C anodes was first clarified by employing *in situ* temperature-dependent Nyquist plots and *ex situ* X-ray photoelectron spectroscopy. It was evidenced that physiochemical evolution of the SEI and surface carbonaceous materials made a significant contribution to the improved sodium storage performance through the following three mechanisms: (1) FeN_x catalyzed the reversible conversion of SEIs, beneficial to the storage and release of extra Na ions, (2) a large number of spin-polarized charges were stored on the surface of the reduced Fe species, and (3) the carbon delivered additional capacity through the surface-capacitive effects. As a result, the FeN_x/C anode provided a high capacity of 217 mA h g⁻¹ after 1000 cycles at 2000 mA g⁻¹. Therefore, the FeN_x/C species catalyzed the reversible conversion reaction of SEIs, which contributed novel avenues to the design of conversion-type electrode materials.

Received 9th September 2021,
Accepted 22nd December 2021

DOI: 10.1039/d1ee02810c

rsc.li/ees

Broader context

The growing demand for energy and the scarcity of fossil fuels are major concerns these days. Thus, the use of renewable energy sources and better energy storage devices attracted much attention. Most studies focused on developing high-performance energy storage devices to meet the ever-increasing demand for energy. One of the main routes is the optimal design of electrodes. Metal–nitrogen–carbon (MN_x/C) nanomaterials attracted considerable attention due to their special properties of high surface areas, which provide a large number of active sites for electrochemical reactions and ion/electron diffusion. In this work, we show that FeN_x/C species can catalyze the reversible conversion reactions of the organic and inorganic ingredients of the SEI, contributing to an enhanced capacity. Furthermore, a large number of spin-polarized electrons were stored on the surface of the reduced Fe species. Therefore, the high-efficiency reversible conversion reaction of the SEI was enabled by FeN_x catalysts, which should be considered as potentially excellent conversion-type materials. Therefore, this work will open a novel route for the electrode design of high-performance MN_x/C species.

Introduction

In recent years, Na-ion batteries (NIBs) serve as one of the most promising large-scale energy storage technologies owing to the natural abundance of sodium resources.¹ The energy density of NIBs is close to that of commercial lithium-ion batteries (LIBs).^{2,3} With the pursuit of batteries with higher energy densities, metal–nitrogen–carbon species attracted more and more attention for their promising electrochemical capacity as anode materials.^{4,5} Among them, FeN_x, as a typical species exhibits a highly reversible capacity, indicating the existence of extra charge reservoirs in the system.⁶ Chen and co-workers proposed that the reversible formation/dissolution of the solid electrolyte interphase (SEI) around the reduced Fe nanoparticles

^a College of Materials Science and Engineering, Zhengzhou University, Zhengzhou 450001, P. R. China. E-mail: zjn@zzu.edu.cn

^b State Key Laboratory of Catalysis, iChEM, Dalian Institute of Chemical Physics, Chinese Academy of Sciences, Dalian 116023, P. R. China. E-mail: dhdeng@dicp.ac.cn

^c Key Laboratory of Chemical Reaction Engineering of Shaanxi Province, College of Chemistry & Chemical Engineering, Yan'an University, Yan'an 716000, P. R. China

^d Center for High Pressure Science and Technology Advanced Research, Pudong, Shanghai 201203, P. R. China

^e Canadian Light Source, 44 Innovation Boulevard Saskatoon, Saskatoon, SK, S7N 2V3, Canada

† Electronic supplementary information (ESI) available. See DOI: 10.1039/d1ee02810c

would lead to an unusually large capacity.⁷ Furthermore, Li *et al.* demonstrated the existence of strong surface capacitance on metal nanoparticles by in-situ XRD and magnetometry analysis, which showed that a large number of spin-polarized electrons were stored in the reduced metallic nanoparticles, making significant contributions to the extra capacity in Fe₃O₄-LIBs.⁸ However, the contribution of the SEI to the unusual capacity of FeN_x has not yet been revisited and clarified in detail.

During SEI reactions, the growth of the SEI is accompanied by electron transfer to form radical anions, and the 3d metals act as catalysts.⁹ Thus, reversible magnetism variation is expected in 3d magnetic metals due to the 3d electron transfers during the formation and decomposition processes of the SEI.¹⁰ Li and co-workers demonstrated that the growth of a low-voltage polymeric film led to the abnormal capacity and reversible formation of spin capacitors.¹¹ Therefore, NIBs were selected as the targets in this work. During the reversible formation/decomposition process of the SEI, it is still a great challenge for the electrode materials to make full use of the high activity of the charge-discharge products and the spin polarization of the products to store additional charges.¹²

Herein, a model anode, a FeN_x/C catalyst with Fe-N_x sites and Fe-N-C-encapsulated Fe₃C nanoparticles, was fabricated

through one-step pyrolysis. The active sites were finely tuned *via* ferric nitrate (Fe source) and polyvinylpyrrolidone (N source for stabilizing the Fe atoms and balancing the Fe content) at a series of temperatures. The well-tailored electronic structure enables FeN_x to exhibit catalytic performance towards the reversible conversion process of the SEI, which contributes to the storage of additional sodium ions. The conversion of the NaF intermediates with surface halides to FeF₃ at the SEI was the key to the enhanced storage capacity provided by Fe atoms. Based on the *ex situ* XPS and *in situ* temperature-dependent Nyquist plot studies, it is confirmed that the extra capacity is provided by the reversible conversion of organic and inorganic ingredients at the SEI. Moreover, the surface capacitance effect and the contribution of the sodium ion intercalation/deintercalation processes on the surface of the carbon-based materials were responsible for the enhanced capacity. A series of characterization methods showed that Fe-N_x was essential for the generation of FeF₃ and the following conversion of the SEI. In addition, the optimized Fe₃C nanoparticles dramatically facilitated this process due to the fast electron-transport kinetics. However, more electrons were processed by further tuning various Fe species, which in turn promoted the generation of the SEI and overwhelmed the generation of unstable

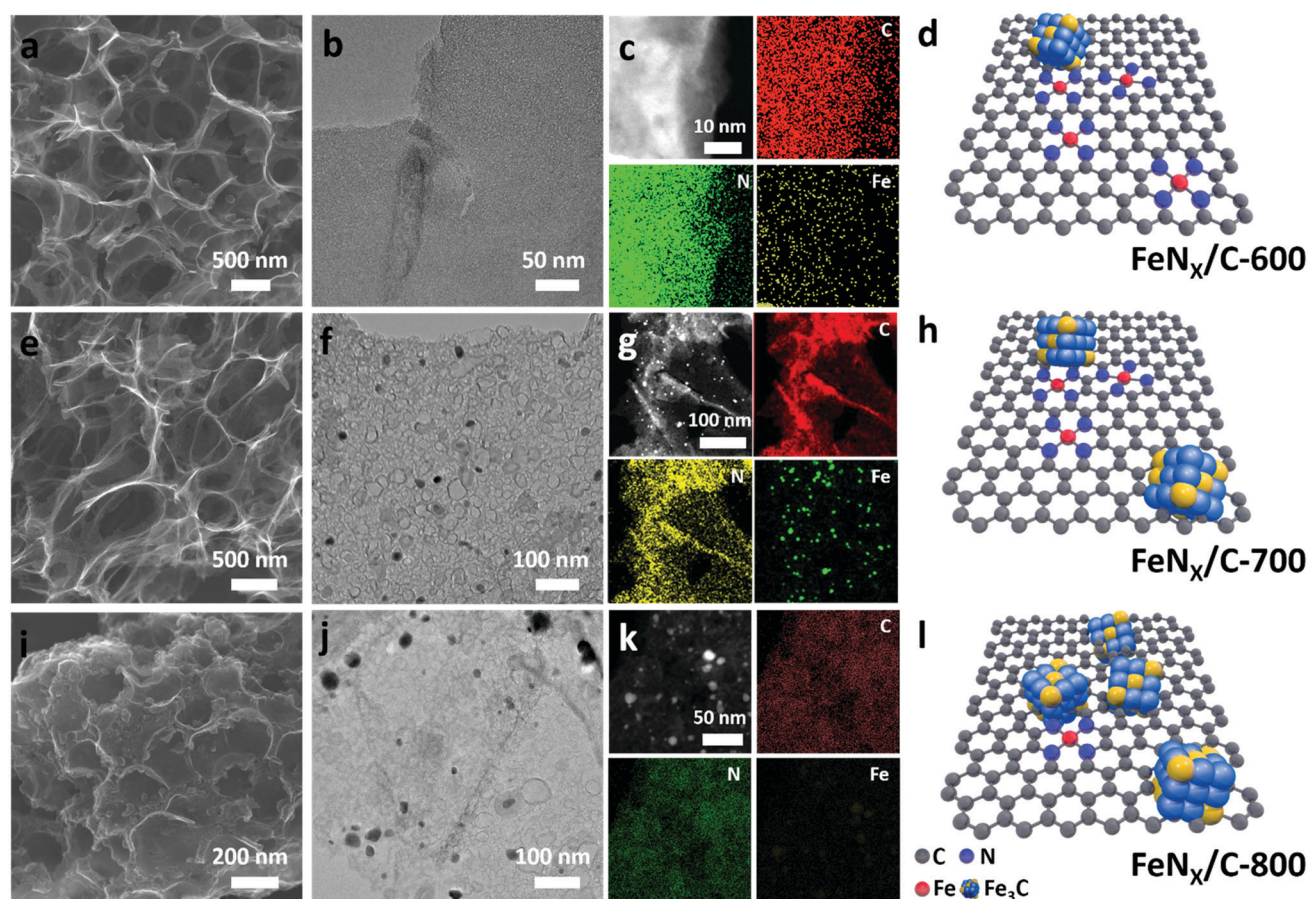


Fig. 1 Morphological characterization. (a) SEM and (b) TEM images, (c) HADDF-STEM EDS mapping, and (d) schematic illustration of model systems of FeN_x/C-600. (e) SEM and (f) TEM images, (g) HADDF-STEM EDS mapping, and (h) schematic illustration of model systems of FeN_x/C-700. (i) SEM and (j) TEM images, (k) HADDF-STEM EDS mapping, and (l) schematic illustration of model systems of FeN_x/C-800.

components. These findings provided guidance for the efficient use of an SEI in electrochemical energy storage.

Results and discussion

Synthesis and characterization

FeN_x/C-*T* (*T* represents the pyrolysis temperature) was synthesized *via* one-step pyrolysis of Fe precursors and PVP at 600, 700, and 800 °C, respectively. X-ray diffraction (XRD) was employed to characterize the crystalline structures of FeN_x/C-*T*. As shown in Fig. S1 (ESI[†]), the primary diffraction peak of FeN_x/C-800 at 25.86° was assigned to the (002) plane of the graphitic carbon.¹³ The diffraction peaks at 37.74°, 42.88°, 43.74°, 45.86°, and 44.6° in the XRD pattern of FeN_x/C-800 were attributed to the (210), (211), (102), and (112) planes of Fe₃C (JCPDS No. 35-0772) and the (110) plane of Fe, respectively.¹⁴ The weak peaks from 35° to 50° in FeN_x/C-700 indicated the existence of a small amount of Fe/Fe₃C species. Furthermore, there was no obvious XRD peak at 600 °C. These results suggested that the content of the Fe/Fe₃C nanoparticles decreased with the decrease of the pyrolysis temperature.

The transmission electron microscopy (TEM) and scanning electron microscopy (SEM) images of FeN_x/C-600 are shown in Fig. 1a and b, and Fig. S3 (ESI[†]), which revealed that FeN_x/C-600 possessed a layered porous structure. Fe, N, and C elements were further identified and mapped out by energy dispersive X-ray spectrometry (EDS) (Fig. 1c). Uniformly distributed C, N and Fe were observed. The result clearly disclosed that Fe atoms were adjacent to the N atoms at the atomic level, suggesting the presence of Fe-N_x species (Fig. 1d). As the pyrolysis temperature increased to 700 °C, the FeN_x/C-700 showed a network structure composed of 2D porous nanosheets (Fig. 1e). Furthermore, Fe₃C nanoparticles were encapsulated with well-crystallized graphene layers (Fig. 1f).¹⁵ The uniformly distributed C and N elements for FeN_x/C-700 and some aggregated Fe elements suggest the presence of Fe-N_x coordination, which overlapped with Fe₃C nanoparticles (Fig. 1g, h, and Fig. S4, ESI[†]).¹⁶ In addition, as the pyrolysis temperature increased to 800 °C, most of Fe aggregated, resulting in more exposed Fe₃C active sites (a lattice distance of 0.21 nm, and the *d*-spacing of (211) planes of Fe₃C) (Fig. 1i, j and Fig. S5, ESI[†]).¹⁷ At the same time, the content of N decreased markedly in FeN_x/C-800, indicating that Fe-N_x sites decreased or transformed into the exposed Fe₃C nanoparticles (Fig. 1k and l).

The Raman spectra of FeN_x/C-600, FeN_x/C-700, and FeN_x/C-800 are shown in Fig. S6 (ESI[†]). The peaks at 1347 cm⁻¹ and 1587 cm⁻¹ represented the D-band of the disordered sp³ carbon and vibrational G-band, respectively.¹⁸ The ratio of the peak intensity (*I*_D/*I*_G) reduced from 1.09 to 0.88 for FeN_x/C-600, FeN_x/C-700, and FeN_x/C-800. The result proved that the increased temperature improved the graphitization degree, which was in line with the XRD results. The N₂ adsorption-desorption isotherms of FeN_x/C-600, FeN_x/C-700, and FeN_x/C-800 are shown in Fig. S7 (ESI[†]). The hysteresis loop in all isotherms

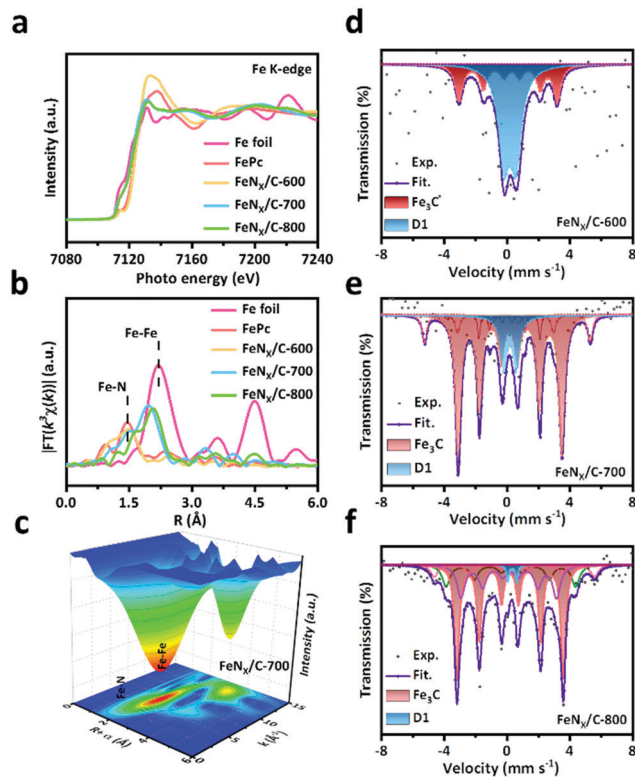


Fig. 2 Structural characterization. (a) K-edge XANES spectra and (b) Fourier transforms of k^3 -weighted K-edge EXAFS spectra of FeN_x/C-600, FeN_x/C-700, FeN_x/C-800, Fe foil, and FePc, respectively. (c) Wavelet transform of the k^3 -weighted EXAFS data of FeN_x/C-700. (d–f) Room-temperature ⁵⁷Fe Mössbauer spectra of FeN_x/C-600, FeN_x/C-700, and FeN_x/C-800, respectively.

corresponds to type IV characterized by typical mesoporous adsorption according to the International Union of Pure and Applied Chemistry (IUPAC) classification (Fig. S7a, ESI[†]).¹⁹ There was no hysteresis effect under relatively low pressure, indicating monolayer adsorption on the mesoporous surface. The specific surface areas (Table S1, ESI[†]) increased and then decreased with the increase of the Fe species content. The specific surface area of FeN_x/C-700 was the largest among the three samples (660 m² g⁻¹), which was attributed to the reduction of the Fe₃C agglomeration by the introduction of the Fe species. However, the introduction of an excess of Fe species resulted in a reduced specific surface area due to the stacking and agglomeration of Fe₃C. The pore size distribution of the samples was evaluated using the adsorption isotherms by the Barrett-Joyner-Halenda (BJH) method (Fig. S7b, ESI[†]). All samples showed relatively large mesopores. In addition, the bonding characteristics and elemental composition of FeN_x/C-600, FeN_x/C-700, and FeN_x/C-800 were further confirmed by XPS (Fig. S9–S11, ESI[†]). The signal at around 711.5 eV was assigned to Fe²⁺ of Fe-N configuration (Fig. S11d, ESI[†]).²⁰ As the temperature increased from 600 °C to 800 °C, the Fe content in Fe-N increased, and the content of Fe-N (398.8 eV) showed an opposite trend. These results were consistent with the XPS results of Fe 2p (Fig. S9c, S10c, and S11c, ESI[†]).

In order to explore the structure–function relationship of the catalysts, Fe K-edge XAS was further used to analyze the coordination environment and valence of the Fe species (Fig. 2a). The valence state of FeN_x/C-600 was close to Fe^{II} divalent according to the Fe K-edge spectrum.²¹ The absorption edge of FeN_x/C-700 shifted to a lower energy, indicating that the valence state of the Fe species in FeN_x/C-700 was lower than that of Fe^{II}, due to the higher electron density than that of FeN_x/C-600 caused by the increase of the Fe₃C nanoparticle content.²² Similarly, FeN_x/C-800 possessed the highest electron density among these anode materials due to the lowest energy. The Fourier transforms of *k*³-weighted Fe K-edge EXAFS spectra are shown in Fig. 2b. The first shell peak of FeN_x/C-600 at around 1.5 Å was assigned to Fe–N, confirming the existence of Fe–N_x.²³ FeN_x/C-700 exhibited a strong peak at around 2.3 Å, which was attributed to the Fe–Fe band.²³ Compared with FeN_x/C-700, FeN_x/C-800 showed a sharp and strong peak at around 2.4 Å. The intensity of the Fe–Fe band in the *R* space increased and Fe–N_x reduced with the increase of the pyrolysis temperature.

Combined with the STEM and XPS results, the Fe–N_x sites of FeN_x/C-700 overlapped with those of the Fe₃C nanoparticles. When the pyrolysis temperature increased to 800 °C, the Fe₃C

nanoparticles intensely overlapped with the Fe–N_x sites in FeN_x/C-800, which promoted the increase of the Fe–N_x electron density at the Fe₃C sites. Due to the powerful resolution in the *k* and *R* spaces, Fe K-edge wavelet transform (WT)-EXAFS was applied to investigate the atomic configurations of FeN_x/C-600, FeN_x/C-700, and FeN_x/C-800 (Fig. 2c and Fig. S12, ESI†).²⁴ By the comprehensive consideration of the Fe–N and Fe–Fe contributions, the WT contour plots of FeN_x/C-700 exhibited the coordination of Fe–N and Fe–Fe.²⁵ Compared with the WT signals of the Fe foil and FePc, there was no obvious coordination between Fe–Fe and Fe–N in FeN_x/C-600 and FeN_x/C-800, which further identified the isolated feature of the Fe species in FeN_x/C.²⁶ The function and contents of different kinds of Fe species were further distinguished by Mössbauer spectroscopy.²⁷ The fitting of Mössbauer parameters and the relative areas of various Fe species are shown in Table S2 (ESI†). The curve of FeN_x/C-600 was fitted with two components (Fig. 2d). The doublet D1 was assigned to the low-spin states of the Fe^{II}–N₄ coordination, and the sextet 1 referred to the Fe₃C species.^{28,29} The curve of FeN_x/C-800 was similar to that of FeN_x/C-700, while the contents of Fe–N and Fe₃C were different (Fig. 2e and f). The content of each Fe species was calculated by combining with ICP-OES measurements, as listed

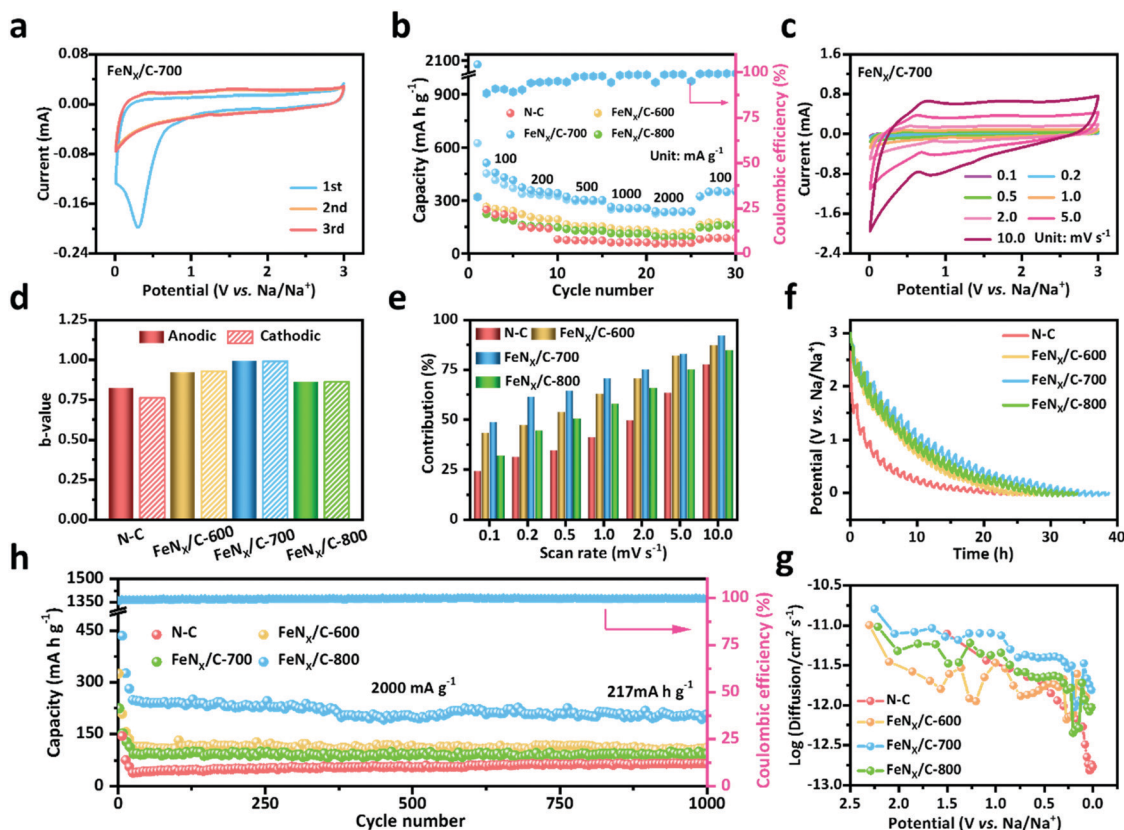


Fig. 3 Electrochemical kinetic behavior. (a) Typical CV curves of the FeN_x/C-700. (b) Rate capability of NC, FeN_x/C-600, FeN_x/C-700, and FeN_x/C-800 electrodes in different electrolytes from 100 to 2000 mA g⁻¹. (c) CV curves of FeN_x/C-700 at scan rates of 0.1–10.0 mV s⁻¹. (d) *b*-Values for the various anodes. (e) Normalized contribution ratios of capacitive capacities of NC, FeN_x/C-600, FeN_x/C-700, and FeN_x/C-800 at different scan rates. (f) The GITT profiles of discharge curves. (g) The diffusion coefficients calculated from GITT profiles as a function of discharge process. (h) Long-term cyclability of NC, FeN_x/C-600, FeN_x/C-700, and FeN_x/C-800 at 2000 mA g⁻¹.

in Table S2 (ESI[†]). The content of Fe–N_x decreased from 65.29% (FeN_x/C-600) to 2.02% (FeN_x/C-800). Among these Fe species, the Fe–N content was high in FeN_x/C-600, but the Fe content in FeN_x/C-600 was low (2.1 wt%), and the Fe–N content was relatively low (1.37 wt%). The content of Fe in FeN_x/C-800 (9.1 wt%) was slightly higher than that of FeN_x/C-700 (8.0 wt%). FeN_x/C-700 possessed more Fe–N (2.05 wt%) and less Fe₃C (5.98 wt%), which led to the lower electron density of FeN_x/C-700 than that of FeN_x/C-800 (Fe–N, 0.18 wt%; Fe₃C, 8.92 wt%). Each sample showed unique properties. In addition, the FeN_x species of the three samples were different in size, which can be used as effective electrode materials for sodium-ion storage. In Fig. S13 (ESI[†]), the magnetic hysteresis curve exhibited that the maximum magnetization values of FeN_x-600, FeN_x-700, and FeN_x-800 were 5.5, 10.5, and 13.5 emu g⁻¹, respectively.

Electrochemical characteristics

The electrochemical characteristics of the FeN_x/C-*T* anodes were studied by cyclic voltammetry (CV), as shown in Fig. 3a and Fig. S14 (ESI[†]). During the initial discharge process, the peaks at around 1.3 V and 0.45 V were assigned to the preliminary formation of the SEI layer, the decomposition of electrolyte and the further reduction of the SEI, respectively.³⁰ In the reverse sweep, due to the catalytic of FeN_x species, a part of SEI undergoes reversible oxidation reaction, leading to a wide peak at 1.75 V.³¹ The rate performance and cycling stability were further investigated to evaluate the electrochemical performance of FeN_x/C-*T*. As shown in Fig. 3b, FeN_x/C-700 possessed the highest rate capacities of 453, 354, 307, 258, and 237 mA h g⁻¹ from 100 mA g⁻¹ to 2000 mA g⁻¹. The discharge capacity recovered to 351 mA h g⁻¹ when the current density was decreased from 2000 mA g⁻¹ to 100 mA g⁻¹, which is attributed to that FeN_x catalyzed the reversible conversion of the SEI. Furthermore, the cycling Coulombic efficiency approaches 100%, showing good reversibility of the reactions.

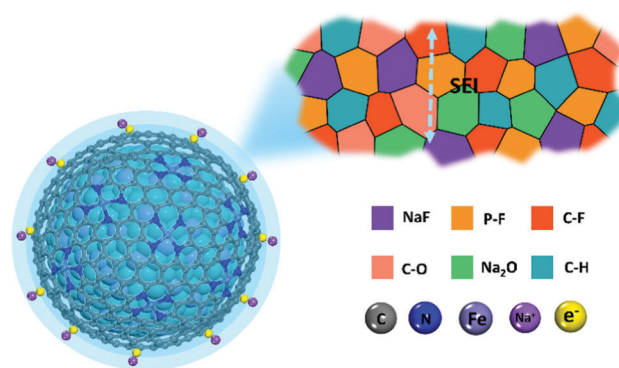
The CV curves of the FeN_x/C-*T* anodes with various scan rates were obtained to quantify the capacity contributions from the total capacitive and diffusion processes (Fig. 3c and Fig. S15, S17, S19, ESI[†]). The results were calculated according to the following equation: $i(V) = k_1V + k_2V^{1/2}$, where $i(V)$ is the total current, and k_1V and $k_2V^{1/2}$ correspond to the surface and diffusion-controlled contributions, respectively (Fig. 3d and Table S3, ESI[†]).³² After the calculations of k_1 and k_2 , the capacitive contribution accounted for 92.1% of the total charge storage at 10 mV s⁻¹ (Fig. 3e), implying that the electrochemical reactions primarily occurred on the surface. The surface-controlled contribution ratios of FeN_x/C-*T* at different scan rates are illustrated in Fig. S16, S18, S20, S22 and Table S4 (ESI[†]). The surface-controlled reaction kinetics gradually increased with the increase of the scan rate, suggesting that the large capacitive contribution on the surface favored the storage of Na ions and gave rise to a high-rate capacity.³³

Galvanostatic intermittent titration technique (GITT) measurements were performed by applying a series of current pulses at 50 mA g⁻¹ for 0.5 h, followed by 0.5 h of the relaxation process, which is aimed at grasping a comprehensive understanding of the diffusion kinetics of Na ions in the N–C, FeN_x/

C-600, FeN_x/C-700, and FeN_x/C-800 electrodes.³⁴ In general, the potential shift during each relaxation period represents the variation of overpotential for the corresponding sodiation stage.³⁵ As shown in Fig. 3f, the FeN_x/C-700 electrode exhibited smaller overpotentials than those of the N–C, FeN_x/C-600, and FeN_x/C-800 electrodes, indicating a higher Na ion diffusion coefficient (D_k).³⁶ The logarithms of the diffusion coefficients *versus* potentials were plotted, as shown in Fig. 3g. The D_k value of the FeN_x/C-700 electrode was higher than those of the N–C, FeN_x/C-600, and FeN_x/C-800 electrodes at all potentials, which meant that FeN_x/C-700 supported a faster diffusion rate of the Na ions, in the presence of the more active sites derived from FeN_x. The FeN_x/C-700 anode delivered a reversible discharge capacity of up to 217 mA h g⁻¹ and Coulombic efficiency of 99% at 2000 mA g⁻¹ after 1000 cycles, demonstrating the high stability of FeN_x with appropriate content (Fig. 3h). The rate capability and long-term capacity of FeN_x/C-700 outperformed those of FeN_x/C-600 and FeN_x/C-800, which was further confirmed by the decrease of the arc radius in the electrochemical impedance spectroscopy (EIS) spectra (Fig. S23, ESI[†]).³⁶ From the XPS spectra of the FeN_x/C-*T* after long-term cycles, it is obvious that a large number of C–C bonds and C=C bonds still exist. Due to the decomposition of the electrolyte and the existence of the binder, there will be C–F bonds and a large number of C–H/C=O (Fig. S24–26, ESI[†]). Through N 1s spectra, it can be seen that there are still a large number of Fe–N bonds during the cycle, which indicates that the structure of MN_x has not been destroyed. During the cycle, Fe species will exist in many forms, Fe^{II} and Fe^{III} will transform into each other, and some Fe⁰ will be generated, meaning that a large number of spin-polarized charges were stored on the surface of the reduced Fe species. As a result, through the structural analysis after the cycles, it can be shown that the Fe species will participate in the charge-discharge reaction, and there has always been the existence of MN_x, as FeN_x catalyzed the reversible conversion of the SEI as mentioned before, which is beneficial to the storage and release of extra Na ions.

Evolution of SEI components under the catalysis of FeN_x

The components, structures, and interfacial structures of the SEI on the FeN_x/C anode surface are illustrated in Scheme 1.



Scheme 1 Schematic illustration of SEI structures and chemistry behind Na ion storage in FeN_x/C.

The SEI layer formed on the electrode surface after the charge-discharge process was observed by TEM. After ten cycles, the thickness of the SEI layer formed on the $\text{FeN}_x/\text{C-700}$ electrode surface after cycling was determined to be ~ 10 nm (Fig. 4a), which was much thinner than those on $\text{FeN}_x/\text{C-600}$, $\text{FeN}_x/\text{C-800}$, and N-C (Fig. S30–S35, ESI[†]). Fig. 4b shows the HRTEM image of the $\text{FeN}_x/\text{C-700}$ electrode after 10 cycles. The mixed amorphous and crystal domains appeared on the whole SEI layer surface. From the observation of TEM, it is obvious that the SEI layer was divided into a light amorphous outer layer and a dark crystalline inorganic inner layer and some randomly distributed NaF islands appeared in the amorphous surface layer, as shown in the orange circle in Fig. 4b.³⁷ C, N, Fe, Na, O, F, and P on the electrode surface were mapped by EDS, and some of these were probably derived from the electrolyte

decomposition and/or permeated into the porous reaction layer (Fig. 4c and Fig. S33, ESI[†]). These results indicated that the introduction of FeN_x stabilized the active interface of the Na/electrolyte and suppressed the consumption of the active Na and electrolyte.

According to Barsoukov's model, Na ions diffused across the liquid electrolyte (LE) and SEI layer, accompanied by the charge transfer at the SEI/electrode interface, and then diffused into the inside of the electrode material.³⁸ Herein, it was assumed that the SEI/electrode interface extended into the inner few-layers of the electrodes, involving different resistances and activation energies, which were determined by fitting the EIS spectra and temperature-dependent resistances (Fig. S36, ESI[†]). Fig. S37 (ESI[†]) shows the *in situ* temperature-dependent EIS spectra of FeN_x after 10 cycles at a rate of 100 mA g^{-1} .

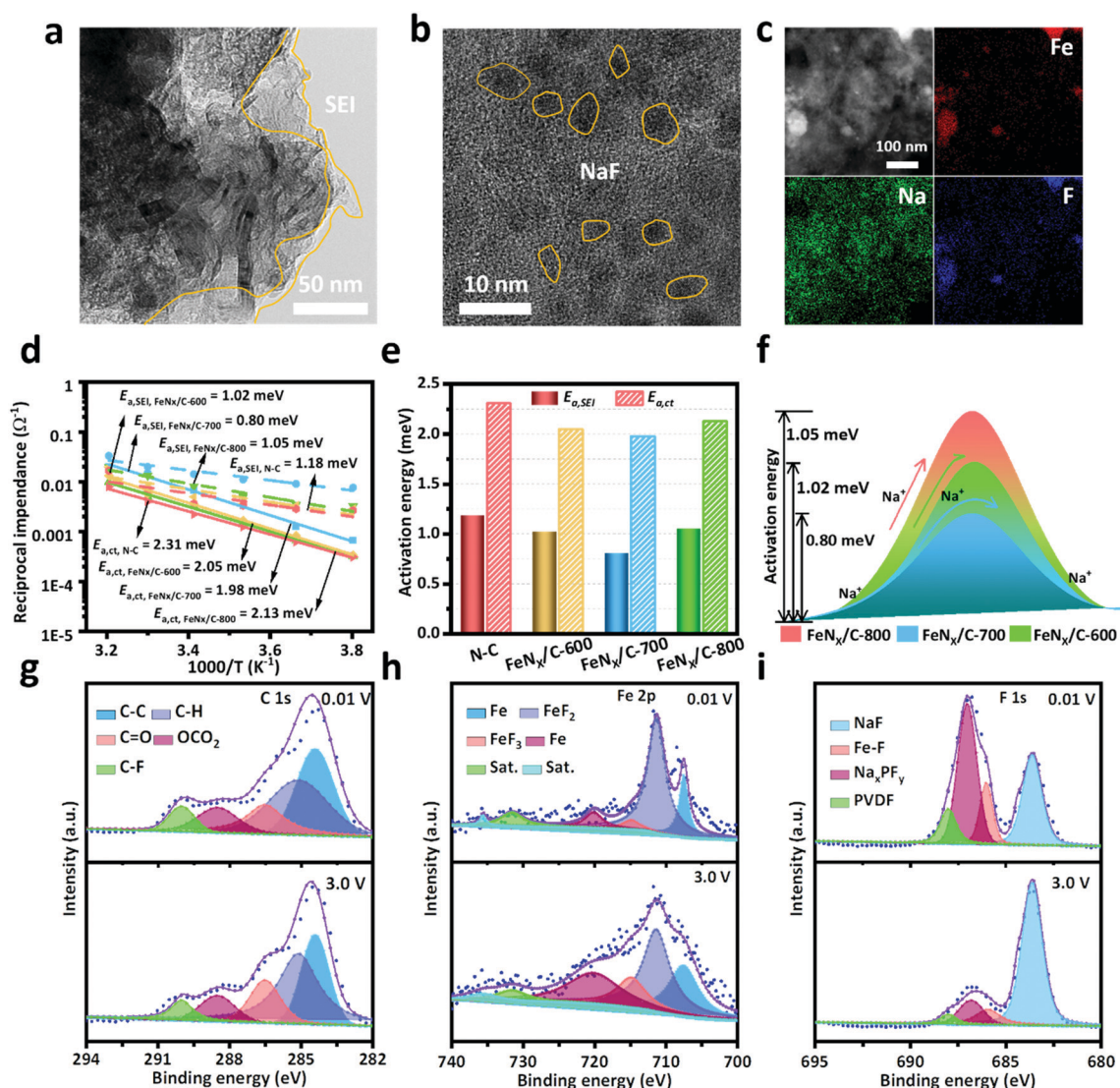


Fig. 4 SEI chemistry and the charge transfer process. Morphological characterization of the SEI layer, (a and b) HRTEM images of $\text{FeN}_x/\text{C-700}$ after 10 cycles. (c) STEM-HAADF images of $\text{FeN}_x/\text{C-700}$ after 10 cycles. (d) Reciprocal bulk and interface impedance as a function of reciprocal temperature; the lines are VFT model fits. (e) The apparent interfacial activation energies obtained from VFT fits of the temperature-dependent reciprocal resistance for various interphase chemistries. (f) The energy barriers for diffusion of Na ions for various electrodes. High-resolution XPS spectra of (g) C 1s, (h) Fe 2p, and (i) F 1s at the SEI on $\text{FeN}_x/\text{C-700}$ at 3 V and 0.01 V.

The temperature dependence of the interfacial ion conductivity can be used to extract information about how the Fe_xC species alters the energy barrier for transportation. The individual contributions of the solid electrolyte interphase (R_{SEI}) and charge transfer resistance (R_{ct}) were obtained by fitting the temperature-dependent impedance spectra based on the equivalent circuit (Table S5, ESI†),³⁹ as shown in Fig. 4d–f. The activation energies of the SEI and SEI/electrode interface can be determined by the Arrhenius equation:⁴⁰ $\sigma T = A \exp(-E_a/k_B T)$, where A is the pre-exponential factor, E_a is the apparent activation energy of ion transportation, k_B is the Boltzmann constant, σ is ionic conductivity, and T is the absolute temperature. As expected, the activation energy of Na ions transportation across the SEI/electrode interface ($E_{a,\text{ct}}$) was higher than those across the SEI layers ($E_{a,\text{SEI}}$) (Fig. 4e). Compared with $\text{FeN}_x/\text{C}-600$ and $\text{FeN}_x/\text{C}-800$, $\text{FeN}_x/\text{C}-700$ had the lowest activation energy ($E_{a,\text{ct}} = 1.98$ meV) as shown in Fig. 4f. Moreover, the $E_{a,\text{SEI}}$ values of all the $\text{FeN}_x/\text{C}-T$ electrodes were lower than those of $E_{a,\text{ct}}$ values, which suggested that the transportation of Na ions across the interface based on the $\text{FeN}_x/\text{C}-700$ electrode was faster than those based on $\text{FeN}_x/\text{C}-600$ and $\text{FeN}_x/\text{C}-800$ electrodes.⁴¹ The fast transportation of Na ions through the SEI/electrode interface resulted in a significant increase in the rate capability, providing crucial insights into the improved interfacial characteristics induced by FeN_x species, as shown in Fig. 4d. The results of the temperature-dependent EIS (Fig. S37, ESI†) also suggested that the charge transfer resistance of the $\text{FeN}_x/\text{C}-700$ anode was always much lower than those of $\text{FeN}_x/\text{C}-600$ and $\text{FeN}_x/\text{C}-800$.

To identify the valence states of the elements and clarify whether the surface Fe species participated in redox reactions, the SEI layer formed on the $\text{FeN}_x/\text{C}-700$ anode surface during the tenth cycle at various potential states was identified by XPS. NaF and Na_2O were detected in the SEI layers (Fig. S27, ESI†). The deconvolution of Fe 2p revealed the characteristic peaks of FeF_3 (714.8 eV) and FeF_2 (711.3 eV), verifying the formation of surface fluoride active sites (Fig. 4h and i).⁷ FeF_3 active sites experienced periodic generation and consumption during the charge and discharge reactions, delivering additional capacity as FeF_3 was recovered to Fe and NaF.⁴² In addition, FeF_3 underwent a pseudocapacitive reaction and was converted to FeF_2 .⁴³ Meanwhile, the proportion of NaF decreased as the potential was increased from 0.1 V to 3.0 V, indicating that inorganic NaF participated in the electrochemical reactions. Corresponding to the XPS spectra of Fe 2p (Fig. 4h), the surface electrons generated by the metal Fe^0 nanoparticles in the charge and discharge processes had a high spin polarization, which stored many spin-polarized electrons and produced a large number of additional capacitances.⁴⁴ To our surprise, the spin-polarized surface capacitance was first observed in MN_x , which provided extra capacity beyond the theoretical value. The C 1s spectrum exhibited five contributions at 284.4, 285.1, 286.5, 289.7, and 292.9 eV, which were assigned to hydrocarbon, carbon-carbon, polyether carbon, carbonyl groups, and polycarbonates, respectively (Fig. 4g).^{43,45–47} After the discharge/charge processes, the decomposition of the electrolyte will lead to the formation of a large number of carbonyl groups.

In the fully charged state, the composition of the SEI layer on the electrode surface was almost constant, but the relative proportion of each species varied due to the catalysis of FeN_x . Further evidence was provided by the electrochemical tests employing $\text{FeN}_x/\text{C}-600$ and $\text{FeN}_x/\text{C}-800$ as the electrodes (Fig. S27–29, ESI†).

Conclusions

In summary, the distinction and mutual effect of the Fe species and active sites on the SEI conversion and accelerating sodium ion diffusion were analyzed using the model anodes consisting of Fe- N_x sites and Fe_3C nanoparticles in this work. Fe_3C nanoparticles, especially Fe_3C with appropriate electrons, boosted the activity of Fe- N_x towards the evolution of the SEI and enhanced the instability of the key components to accelerate further SEI conversion. Furthermore, the electrochemically reduced Fe species stored a large number of spin-polarized electrons, which resulted in extra capacity. The surface carbon delivered additional capacity through a surface-controlled capacitive effect. Therefore, the well-prepared $\text{FeN}_x/\text{C}-700$ anode can provide a high capacity of 217 mA h g^{-1} and a Coulombic efficiency of 99% after 1000 cycles at 2000 mA g^{-1} . An in-depth understanding of the active sites on the conversion of the SEI clarified in this work will provide guidelines for the use of efficient anode materials in electrochemical energy storage.

Author contributions

X. H. C. performed the materials preparation, characterization and studied the performance. Z. L. X., W. Y. F., T. Y. C., D. H. L., H. Y. F., Q. G., Y. Y., and Z. K. X. assisted the materials preparation and data analysis. Z. J. N. and D. D. H. supervised the project.

Conflicts of interest

There are no conflicts to declare.

Acknowledgements

This work was supported financially by the National Key R&D Program of China (No. 2016YFA0204100, and 2016YFA0200200), the National Natural Science Foundation of China (No. 21875221, 21988101, 21890753, and 22162026), the Strategic Priority Research Program of Chinese Academy of Sciences (XDB36030200), the Danish company Haldor Topsøe A/S, the Youth Talent Support Program of High-Level Talents Special Support Plan in Henan Province (ZYQR201810148), and Creative Talents in the Education Department of Henan Province (19HAS-TIT039). We thank the staff at the BL14W1 beamline of the Shanghai Synchrotron Radiation Facilities (SSRF) and the 4B9A beamline of Beijing Synchrotron Radiation Facility (BSRF) for assistance with the EXAFS and XANES measurements. We also

acknowledge the Center for Advanced Mössbauer Spectroscopy, Dalian Institute of Chemical Physics, CAS, for providing the Mössbauer measurements and analysis.

Notes and references

- 1 M. Armand and J. M. Tarascon, *Nature*, 2008, **451**, 652–657.
- 2 W. Cai, Y. X. Yao, G. L. Zhu, C. Yan, L. L. Jiang, C. He, J. Q. Huang and Q. Zhang, *Chem. Soc. Rev.*, 2020, **49**, 3806–3833.
- 3 Q. Liu, Y. Wang, X. Yang, D. Zhou, X. Wang, P. Jaumaux, F. Kang, B. Li, X. Ji and G. Wang, *Chem*, 2021, **7**, 1993–2021.
- 4 X. He, D. Bresser, S. Passerini, F. Baakes, U. Krewer, J. Lopez, C. T. Mallia, Y. Shao-Horn, I. Cekic-Laskovic, S. Wiemers-Meyer, F. A. Soto, V. Ponce, J. M. Seminario, P. B. Balbuena, H. Jia, W. Xu, Y. B. Xu, C. M. Wang, B. Horstmann, R. Amine, C. C. Su, J. Y. Shi, K. Amine, M. Winter, A. Latz and R. Kostecki, *Nat. Rev. Mater.*, 2021, **6**, 1036–1052.
- 5 C. Lu, R. Fang and X. Chen, *Adv. Mater.*, 2020, **32**, e1906548.
- 6 T. Sun, S. Mitchell, J. Li, P. Lyu, X. Wu, J. Perez-Ramirez and J. Lu, *Adv. Mater.*, 2020, **32**, e2003075.
- 7 D. J. Chen, C. Feng, Y. P. Han, B. Yu, W. Chen, Z. Q. Zhou, N. Chen, J. B. Goodenough and W. D. He, *Energy Environ. Sci.*, 2020, **13**, 2924–2937.
- 8 Q. Li, H. Li, Q. Xia, Z. Hu, Y. Zhu, S. Yan, C. Ge, Q. Zhang, X. Wang, X. Shang, S. Fan, Y. Long, L. Gu, G. X. Miao, G. Yu and J. S. Moosera, *Nat. Mater.*, 2021, **20**, 76–83.
- 9 G. Gershinsky, E. Bar, L. Monconduit and D. Zitoun, *Energy Environ. Sci.*, 2014, **7**, 2012–2016.
- 10 N. A. Chernova, G. M. Nolis, F. O. Omenya, H. Zhou, Z. Li and M. S. Whittingham, *J. Mater. Chem.*, 2011, **21**, 9865.
- 11 H. Li, Z. Hu, Q. Xia, H. Zhang, Z. Li, H. Wang, X. Li, F. Zuo, F. Zhang, X. Wang, W. Ye, Q. Li, Y. Long, Q. Li, S. Yan, X. Liu, X. Zhang, G. Yu and G. X. Miao, *Adv. Mater.*, 2021, **33**, e2006629.
- 12 A. Hu, W. Chen, X. Du, Y. Hu, T. Lei, H. Wang, L. Xue, Y. Li, H. Sun, Y. Yan, J. Long, C. Shu, J. Zhu, B. Li, X. Wang and J. Xiong, *Energy Environ. Sci.*, 2021, **14**, 4115–4124.
- 13 J. Xiao, J. Han, C. Zhang, G. Ling, F. Kang and Q. H. Yang, *Adv. Energy Mater.*, 2021, **11**, 2100775.
- 14 Y. Xing, Z. Yao, W. Li, W. Wu, X. Lu, J. Tian, Z. Li, H. Hu and M. Wu, *Angew. Chem., Int. Ed.*, 2021, **60**, 8889–8895.
- 15 D. Deng, L. Yu, X. Chen, G. Wang, L. Jin, X. Pan, J. Deng, G. Sun and X. Bao, *Angew. Chem., Int. Ed.*, 2013, **52**, 371–375.
- 16 Y. Qiao, P. Yuan, Y. Hu, J. Zhang, S. Mu, J. Zhou, H. Li, H. Xia, J. He and Q. Xu, *Adv. Mater.*, 2018, **30**, e1804504.
- 17 J. Zhang, K. Wang, Q. Xu, Y. Zhou, F. Cheng and S. Guo, *ACS Nano*, 2015, **9**, 3369–3376.
- 18 A. C. Ferrari and D. M. Basko, *Nat. Nanotechnol.*, 2013, **8**, 235–246.
- 19 E. P. Barrett, L. G. Joyner and P. P. Halenda, *J. Am. Chem. Soc.*, 1951, **73**, 373–380.
- 20 T. Marshall-Roth, N. J. Libretto, A. T. Wrobel, K. J. Anderton, M. L. Pegis, N. D. Rieke, T. V. Voorhis, J. T. Miller and Y. Surendranath, *Nat. Commun.*, 2020, **11**, 5283.
- 21 A. Zitolo, V. Goellner, V. Armel, M. T. Sougrati, T. Mineva, L. Stievano, E. Fonda and F. Jaouen, *Nat. Mater.*, 2015, **14**, 937–942.
- 22 Q. Chang, C. Zhang, C. Liu, Y. Wei, A. V. Cheruvathur, A. I. Dugulan, J. W. Niemantsverdriet, X. Liu, Y. He, M. Qing, L. Zheng, Y. Yun, Y. Yang and Y. Li, *ACS Catal.*, 2018, **8**, 3304–3316.
- 23 G. Yang, J. Zhu, P. Yuan, Y. Hu, G. Qu, B. A. Lu, X. Xue, H. Yin, W. Cheng, J. Cheng, W. Xu, J. Li, J. Hu, S. Mu and J. N. Zhang, *Nat. Commun.*, 2021, **12**, 1734.
- 24 H. Funke, M. Chukalina and A. C. Scheinost, *J. Synchrotron Radiat.*, 2007, **14**, 426–432.
- 25 H. Xia, P. Yuan, L. Zan, G. Qu, Y. Tu, K. Zhu, Y. Wei, Z. Wei, F. Zheng, M. Zhang, Y. Hu, D. Deng and J. Zhang, *Nano Res.*, 2021, DOI: 10.1007/s12274-021-3992-9.
- 26 H. Funke, M. Chukalina and A. Rossberg, *Phys. Scr.*, 2005, **T115**, 232–234.
- 27 H. Zhang, H. T. Chung, D. A. Cullen, S. Wagner, U. I. Kramm, K. L. More, P. Zelenay and G. Wu, *Energy Environ. Sci.*, 2019, **12**, 2548–2558.
- 28 L. Jiao, J. Li, L. L. Richard, Q. Sun, T. Stracensky, E. Liu, M. T. Sougrati, Z. Zhao, F. Yang, S. Zhong, H. Xu, S. Mukerjee, Y. Huang, D. A. Cullen, J. H. Park, M. Ferrandon, D. J. Myers, F. Jaouen and Q. Jia, *Nat. Mater.*, 2021, **20**, 1385–1391.
- 29 J. Li, M. T. Sougrati, A. Zitolo, J. M. Ablett, I. C. Oğuz, T. Mineva, I. Matanovic, P. Atanassov, Y. Huang, I. Zenyuk, A. Di Cicco, K. Kumar, L. Dubau, F. Maillard, G. Dražić and F. Jaouen, *Nat. Catal.*, 2020, **4**, 10–19.
- 30 W. Liu, P. Liu and D. Mitlin, *Adv. Energy Mater.*, 2020, **10**, 2002297.
- 31 N. Takenaka, A. Bouibes, Y. Yamada, M. Nagaoka and A. Yamada, *Adv. Mater.*, 2021, **33**, e2100574.
- 32 X. Pu, D. Zhao, C. Fu, Z. Chen, S. Cao, C. Wang and Y. Cao, *Angew. Chem., Int. Ed.*, 2021, **60**, 2.
- 33 V. A. Nikitina, S. Y. Vassiliev and K. J. Stevenson, *Adv. Energy Mater.*, 2020, **10**, 1903933.
- 34 M. Kim, D. C. Robertson, D. W. Dees, K. P. Yao, W. Lu, S. E. Trask, J. T. Kirner and I. Bloom, *J. Electrochem. Soc.*, 2021, **168**, 070506.
- 35 Y. Zhu and C. Wang, *J. Phys. Chem. C*, 2010, **114**, 2830–2841.
- 36 K. Tang, X. Yu, J. Sun, H. Li and X. Huang, *Electrochim. Acta*, 2011, **56**, 4869–4875.
- 37 M. Ma, H. Cai, C. Xu, R. Huang, S. Wang, H. Pan and Y. S. Hu, *Adv. Funct. Mater.*, 2021, **32**, 2100278.
- 38 E. Barsoukov, J. H. Kim, J. H. Kim, C. O. Yoon and H. Lee, *J. Electrochem. Soc.*, 2019, **145**, 2711–2717.
- 39 K. Li, J. Zhang, D. Lin, D. W. Wang, B. Li, W. Lv, S. Sun, Y. B. He, F. Kang, Q. H. Yang, L. Zhou and T. Y. Zhang, *Nat. Commun.*, 2019, **10**, 725.
- 40 M. R. Busche, T. Drossel, T. Leichtweiss, D. A. Weber, M. Falk, M. Schneider, M. L. Reich, H. Sommer, P. Adelhelm and J. Janek, *Nat. Chem.*, 2016, **8**, 426–434.
- 41 M. Gaberscek, *Nat. Commun.*, 2021, **12**, 6513.
- 42 D.-l. Ma, H.-g. Wang, Y. Li, D. Xu, S. Yuan, X.-l. Huang, X.-b. Zhang and Y. Zhang, *Nano Energy*, 2014, **10**, 295–304.

- 43 C. Li, C. Yin, L. Gu, R. E. Dinnebier, X. Mu, P. A. van Aken and J. Maier, *J. Am. Chem. Soc.*, 2013, **135**, 11425–11428.
- 44 Z. Li, Y. Zhang, X. Li, F. Gu, L. Zhang, H. Liu, Q. Xia, Q. Li, W. Ye, C. Ge, H. Li, H. Hu, S. Li, Y. Z. Long, S. Yan, G. X. Miao and Q. Li, *J. Am. Chem. Soc.*, 2021, **143**, 12800–12808.
- 45 P. Qin, M. Wang, N. Li, H. Zhu, X. Ding and Y. Tang, *Adv. Mater.*, 2017, **29**, 1606805.
- 46 X. Han, G. Xu, Z. Zhang, X. Du, P. Han, X. Zhou, G. Cui and L. Chen, *Adv. Energy Mater.*, 2019, **9**, 1804022.
- 47 H. Wang and Y. Tang, *Chem. Res. Chin. Univ.*, 2020, **36**, 402–409.